Geophysical Journal International

Geophys. J. Int. (2009) **179,** 1414–1428 doi: 10.1111/j.1365-246X.2009.04361.x

Modelling the palaeo-evolution of the geodynamo

Julien Aubert,[1] Stéphane Labrosse[2] and Charles Poitou[3]

[1] *Dynamique des Fluides Géologiques, Institut de Physique du Globe de Paris, Université Paris-Diderot, INSU/CNRS,* 4 *Place Jussieu,* 75252, *Paris cedex* 05, *France. E-mail: aubert@ipgp.jussieu.fr*

[2] *Laboratoire des sciences de la Terre, Ecole normale supérieure de Lyon, Université de Lyon, CNRS UMR* 5570, 46 *Allée d'Italie,* 69364 *Lyon Cedex* 07, *France*

[3] *Paléomagnétisme, Institut de Physique du Globe de Paris, Université Paris-Diderot, INSU/CNRS,* 4 *Place Jussieu,* 75252, *Paris cedex* 05, *France*

Accepted 2009 August 11. Received 2009 May 22; in original form 2008 December 10

SUMMARY

Although it is known that the geodynamo has been operating for at least 3.2 Ga, it remains difficult to infer the intensity, dipolarity and stability (occurrence of reversals) of the Precambrian magnetic field of the Earth. In order to assist the interpretation of palaeomagnetic data, we produce models for the long-term evolution of the geodynamo by combining core thermodynamics with a systematic scaling analysis of numerical dynamo simulations. We update earlier dynamo scaling results by exploring a parameter space, which has been extended in order to account for core aspect ratios and buoyancy source distributions relevant to Earth in the Precambrian. Our analysis highlights the central role of the convective power, which is an output of core thermodynamics and the main input of our updated scalings. As the thermal evolution of the Earth's core is not well known, two end-member models of heat flow evolution at the core–mantle boundary (CMB) are used, respectively, terminating at present heat flows of 11 TW (high-power scenario) and 3 TW (low power scenario). The resulting models predict that until the appearance of the inner core, a thermal dynamo driven only by secular cooling, and without any need for radioactive heating, can produce a dipole moment of strength comparable to that of the present field, thus precluding an interpretation of the oldest palaeomagnetic records as evidence of the inner core presence. The observed lack of strong long-term trends in palaeointensity data throughout the Earth's history can be rationalized by the weakness of palaeointensity variations predicted by our models relatively to the data scatter. Specifically, the most significant internal magnetic field increase which we predict is associated to the sudden power increase resulting from inner core nucleation, but the dynamo becomes deeper-seated in the core, thus largely cancelling the increase at the core and Earth surface, and diminishing the prospect of observing this event in palaeointensity data. Our models additionally suggest that the geodynamo has lied close to the transition to polarity reversals throughout its history. In the Precambrian, we predict a dynamo with similar dipolarity and less frequent reversals than at present times, due to conditions of generally lower convective forcing. Quantifying the typical CMB heat flow variation needed for the geodynamo to cross the transition from a reversing to a non-reversing state, we find that it is unlikely that such a variation may have caused superchrons in the last 0.5 Ga without shutting down dynamo action altogether.

Key words: Dynamo: theories and simulations; Palaeointensity; Palaeomagnetic secular variation; Reversals: process, timescale, magnetostratigraphy.

1 INTRODUCTION

Palaeomagnetic records can be used in order to shed light onto the past of the Earth's dynamo. However, with increasing age, rock sequences are likely to be affected by weathering, alteration and metamorphism, thus destroying the pristine information on the early magnetic field. Although the situation constantly improves with newer samples and better techniques, especially regarding palaeointensity determinations (see Tauxe & Yamazaki 2007, for a review), uncertainties remain concerning the key characteristics of the geodynamo in the Precambrian. A first quantity of interest is the dipole moment. The oldest (3.2 Ga BP) reliable palaeointensity record to date (Tarduno *et al.* 2007) reveals that the virtual dipole moment (VDM) was possibly as large as its present value of 8×10^{22} A m^2, although the consideration of the experimental cooling rate effect may lead to a twofold decrease in the determined VDM. As a

result, the debate concerning the long-term evolution of the VDM remains lively (Dunlop & Yu 2004), though there are suggestions (Macouin *et al.* 2004) of a long-term average monotonous increase from 3×10^{22} A m^2 at 1000–2000 Myr to 8×10^{22} A m^2 at present times. In addition, although it has been proposed (Stevenson *et al.* 1983; Hale 1987) that the power increase subsequent to inner core nucleation and onset of chemical convection in the core could cause a sudden increase in the dipole moment, it appears that until now, the palaeomagnetic data scatter has prevented a proper resolution of this feature. A second quantity of interest is the dipolarity of the field, which can be assessed (McFadden *et al.* 1991) through the analysis of latitude dependence in palaeosecular variation (PSV). Following this line, Smirnov & Tarduno (2004) proposed that the dipolarity should have been higher some 2.5 Ga ago. However, the existence of antipodal directions, which would be a clear evidence of high dipolarity (Dunlop & Yu 2004), is lacking in their data, and more generally, there are considerable issues with this method (Hulot & Gallet 1996), including the difficulty to separate the dipolarity effect from the secular variation effect in the PSV. The PSV can indeed also be used to study the intrinsic variability of the geomagnetic pole, as recently done by Biggin *et al.* (2008), who found evidence of a more stable dynamo 2.4–2.8 Ga ago. This led to the suggestion that a third quantity of interest, the reversal frequency of the geodynamo, was lower at that time than at present. The same conclusion was reached for the last 500 Myr (Eide & Torsvik 1996) through direct magnetostratigraphic analysis, which is obviously a more robust method when data is available, but some contrary indications of high reversal frequency have also been reported for the same period (Pavlov & Gallet 2001). It should be noted however that the strongest signal on the reversal frequency curve is related to the irregular occurrence of superchrons (see for instance, Pavlov & Gallet 2005), where reversal frequency goes down to zero. A last important palaeomagnetic result is the timing of the oldest known reversal, which apparently occurred 2.7 Ga ago (Strik *et al.* 2003), though there are some indications of reversals occurring 3.2 Ga ago (Tarduno *et al.* 2007).

As none of the debate presented above is currently settled, the goal of this study is to gain insight from the comparison of palaeomagnetic results with synthetic time evolution models for the dipolarity, intensity and stability of the Precambrian Earth dynamo. Since a few years, a scaling theory (Christensen & Tilgner 2004; Christensen & Aubert 2006; Olson & Christensen 2006) is available to predict the main characteristic quantities of the present-day geodynamo and planetary dynamos. The central control variable in almost all scalings is the convective buoyancy flux, which is equivalent to convective power available for the dynamo. Thus, in order to achieve scaling predictions relevant to the Precambrian Earth dynamo, one needs a time-series of the dynamo power, which can be evaluated from core thermodynamics and Earth cooling histories (e.g. Labrosse 2003; Lister 2003). Furthermore, the results of Christensen & Tilgner (2004), Christensen & Aubert (2006) and Olson & Christensen (2006) need to be extended to cases where the outer core aspect ratio varies, and where the partitioning between the inner- and outer-boundary originated buoyancies also varies. In these respects, this paper takes advantage of advances made in both fields of numerical dynamo modelling and core thermodynamics to update a previous analytical treatment (Olson 1981). In Section 2, we introduce the numerical dynamo model, which we use for our systematic parameter space study. The numerical results are presented in Section 3.1. Then we turn to the investigation of various Earth cooling histories, and how they relate to the dynamo power (Section 3.2). Finally, we produce our time evolution model for palaeomagnetic observables (Section 3.3) and discuss the results in light of the palaeomagnetic observations and geophysical constraints (Section 4).

2 MODEL

2.1 Outline

We consider an electrically conducting, incompressible fluid in a self-gravitating spherical shell between radii r_i and r_o. The shell is rotating about an axis $\mathbf{e}_z$ with an angular velocity Ω, and convecting thermally and chemically. We study the Earth's core at various stages of its existence, hence its rotation rate, aspect ratio $\chi = r_\mathrm{i}/r_\mathrm{o}$ and thermochemical buoyancy partitioning are variable over geological times, but can be assumed to be constant control parameters over timescales relevant for core dynamics. We define the deviation temperature field T' and light element mass fraction field ξ' with respect to the isentropic temperature and well-mixed mass fraction, and, within the Boussinesq approximation, both buoyancy effects are grouped into a codensity (or density anomaly) field (Braginsky & Roberts 1995) C such that

$$C = \alpha\rho T' + \Delta\rho\xi'. \tag{1}$$

Here α is the thermal expansion coefficient, ρ is the fluid density and $\Delta\rho$ is the density difference between the light components that contribute to chemical convection and pure iron. The temperature and molar fraction fields are assumed to have the same diffusivity κ, due to turbulent mixing in the outer core. This allows us to write a single transport equation for the codensity C, which is solved numerically in a dimensionless form, together with the magnetic induction equation for the solenoidal magnetic field $\mathbf{B}$ in the magnetohydrodynamic approximation, and the Navier–Stokes and thermochemical transport equations for the incompressible velocity field $\mathbf{u}$, and pressure P

$$\frac{\partial \mathbf{u}}{\partial t} + \mathbf{u}\cdot\nabla\mathbf{u} + 2\mathbf{e}_z \times \mathbf{u} + \nabla P = Ra_Q \frac{\mathbf{r}}{r_o} C + (\nabla \times \mathbf{B}) \times \mathbf{B} + E\nabla^2\mathbf{u} \tag{2}$$

$$\frac{\partial \mathbf{B}}{\partial t} = \nabla \times (\mathbf{u} \times \mathbf{B}) + \frac{E}{Pm}\nabla^2\mathbf{B} \tag{3}$$

$$\frac{\partial C}{\partial t} + \mathbf{u}\cdot\nabla C = \frac{E}{Pr}\nabla^2 C + S_{T/\xi} \tag{4}$$

$$\nabla\cdot\mathbf{u} = 0 \tag{5}$$

$$\nabla\cdot\mathbf{B} = 0. \tag{6}$$

Here $\mathbf{r}$ is the radius vector. Time is scaled with the inverse of the rotation rate Ω^{-1}. Length is scaled with the shell gap $D = r_\mathrm{o} - r_\mathrm{i}$. Velocity is scaled with $\Omega\, D$. Magnetic induction is scaled by $(\rho\mu)^{1/2}\Omega D$, where ρ is the fluid density and μ the magnetic permeability of the fluid. The Ekman number E, magnetic Prandtl and Prandtl numbers Pm and Pr are defined as

$$E = \frac{\nu}{\Omega D^2} \tag{7}$$

$$Pm = \frac{\nu}{\lambda} \tag{8}$$

$$Pr = \frac{\nu}{\kappa}. \tag{9}$$

Here ν, λ are, respectively, the viscous and magnetic diffusivities of the fluid. In this study, the codensity boundary conditions relevant to thermochemical convection are treated in the following way: at the inner-core boundary, the release of latent heat and light elements correspond to a positive mass anomaly flux F_i (expressed in kilograms per second), which we consider uniform and imposed on the long term by global core thermodynamics. The dimensional form of F_i writes

$$F_\mathrm{i} = -\int_{S_\mathrm{i}} \kappa \nabla C \cdot \mathbf{dS}, \tag{10}$$

where S_i is the inner boundary surface. Similarly, at the outer boundary, we consider that the mantle imposes a uniform mass anomaly flux (which in fact corresponds to a heat flux without chemical contributions). The dimensional form of F_o writes

$$F_\mathrm{o} = -\int_{S_\mathrm{o}} \kappa \nabla C \cdot \mathbf{dS}. \tag{11}$$

Here S_o is the outer boundary surface. Note that F_o is defined with respect to the adiabatic heat flux carried out at the outer boundary (this is the reference state of the Boussinesq system). Hence, F_o can be either positive or negative, but in any case the total mass anomaly flux $F = F_\mathrm{i} + F_\mathrm{o}$ must be positive for convection to occur. The codensity is scaled with $F/4\pi D^3\Omega$. The Rayleigh number based on mass anomaly flux, Ra_Q, which appears in (2) is therefore defined as

$$Ra_Q = \frac{g_\mathrm{o} F}{4\pi\rho\Omega^3 D^4}. \tag{12}$$

Here g_o is gravity at radius $r = r_\mathrm{o}$. The present formulation is slightly different from, but equivalent to that in Christensen & Aubert (2006), where a Rayleigh number based on advected buoyancy flux Ra_Q^* was introduced. For sufficiently supercritical convection the conversion from their formalism to ours can be achieved through

$$Ra_Q \approx \frac{r_\mathrm{o} r_\mathrm{i}}{D^2} Ra_Q^*. \tag{13}$$

The reason for introducing this change of formulation is that Ra_Q^* is singular in the case where the inner core is not present.

In Section 3.1, we carry out a systematic analysis of the Boussinesq system and let the mass anomaly fluxes F_i and F_o be independent. The two associated control parameters are the Rayleigh number Ra_Q and the fraction of inner-boundary originated buoyancy $f_\mathrm{i} = F_\mathrm{i}/F$. However, we emphasize that in the Earth's core, F_i and F_o are related through a consideration of the complete core thermodynamics, such as done in Sections 3.2 and 3.3. A general situation describing an Earth system which is slowly cooling on geological timescales is $F_\mathrm{i} \neq F_\mathrm{o}$, in which case the basic state over which the Boussinesq system is considered has a decreasing temperature and increasing light element mass fraction, while the Boussinesq system itself is statistically stationary. This can be accounted for within our framework by adding a volumetric correction term $S_{T/\xi}$ in (4), such that the mass anomaly budget of the spherical shell vanishes (Braginsky & Roberts 1995; Kutzner & Christensen 2002). The correction term then has the following dimensionless expression:

$$S_{T/\xi} = 3\frac{(1-2f_\mathrm{i})}{r_\mathrm{o}^3 - r_\mathrm{i}^3}. \tag{14}$$

The other boundary conditions at both boundaries are of rigid type for velocity, and insulating for the magnetic field (the effect on inner-core conductivity on the long-term behaviour of dynamo simulations has been found to be negligible, as shown by Wicht 2002). The numerical implementation PARODY-JA is used in this study (see Aubert *et al.* 2008, for details). The numerical scheme is of finite-differencing type in the radial direction with up to 120 grid points, and uses a spherical harmonic decomposition in the lateral directions up to degree and order 106. No particular symmetry along longitude was assumed.

Table 1 gives details on the 43 models which we have integrated for this study. The parameter range is $E = 3 \times 10^{-5}$ to 3×10^{-4} for the Ekman number, $Ra_Q = 10^{-6}$ to 10^{-3} for the Rayleigh number, $Pm = 1$–10 for the magnetic Prandtl number, and the Prandtl number Pr is set to 1 in all simulations. It should be kept in mind that due to computational limitations, and just like all accessible numerical dynamo simulations (Christensen & Aubert 2006), our simulations operate in a parametric regime still very far from that of the Earth's core, where $E \approx 3 \times 10^{-15}$, $Ra_Q \approx 10^{-13}$ and $Pm = 10^{-6}$. Scaling analyses attempt to overcome this intrinsic limitation by identifying robust trends supported by reasonable underlying physical considerations. Most of the scalings used here bear little residual influence of the various diffusivities, which gives credence to their applicability to core conditions, since diffusivities represent the main reason why models and Earth are distant in parameter space. The models presented here explore the new parameter space axes relative to χ and f_i. The aspect ratio goes down to $\chi = 0.01$, where the inner core is practically non-existent in the simulation. This situation is meant to simulate the core before or at the inner core nucleation time. The geophysically relevant buoyancy driving mode is therefore secular cooling ($f_\mathrm{i} = 0$), which, in our formalism, corresponds to no buoyancy at the inner boundary, a positive volumetric source term, and a fixed heat flow at the outer boundary. Several models have been computed at $\chi = 0.05$, where f_i has been set to 0, 0.5 and 1. These cases correspond to a system where the inner core has just nucleated, and the buoyancy driving is therefore a mix of secular cooling and chemical convection. Finally, models with $\chi = 0.35$ were also needed for comparison with present Earth. Core thermodynamics predict that the main buoyancy source of the present-day geodynamo (in terms of available power) is chemical convection (Lister & Buffett 1995). For that reason, cases with $f_\mathrm{i} = 0$, $\chi = 0.35$ are left out of the present study. However, the uncertainties pertaining to the determination of core–mantle boundary (CMB) heat flow (Lay *et al.* 2008) and core adiabat leave some room for the determination of f_i. Here we use the published runs from Christensen & Tilgner (2004), Christensen & Aubert (2006) and Olson & Christensen (2006), which have been performed with fixed temperature boundary conditions. In our formalism, this is roughly equivalent to $f_\mathrm{i} = 0.5$ (see Fig. 1). In addition, we have included models with $f_\mathrm{i} = 1$, and also with $f_\mathrm{i} = 2$, 10, describing situation of dominant chemical convection where the CMB heat flow is, respectively, just adiabatic, or below the adiabat. In the latter case, a stably stratified layer exists at the top of the outer core.

We define several outputs, which are all averaged over times much longer than core flow timescales (but shorter than geological timescales for Earth's mantle variations), and over the full volume of the spherical shell or the surface of the outer boundary. Most of these bear the same definitions as in Christensen & Aubert (2006): the root-mean-squared velocity inside the shell *Ro*, rms magnetic field amplitude inside the shell *Lo*, mean harmonic degree in the velocity field $\bar{l}$, ohmic dissipation fraction of the convective power f_ohm, ratio b_dip of the mean field strength inside the shell *Lo* to the dipole strength on the outer boundary B_dip, and ratio f_dip of B_dip to the rms amplitude of the magnetic field at the outer boundary truncated at spherical harmonic degree 12. Parameters with definitions which are

Table 1. Numerical models and results (see text for details). Models C and T are visualized in Fig. 2.

	E	Ra_Q	Pr	Pm	χ	f_i	Ro	Lo	b_{dip}	f_{dip}	$\bar{l}$	τ_{diss}/τ_{mag}	p	f_{ohm}
	3×10^{-5}	1.80×10^{-6}	1	1	0.05	0.5	5.03×10^{-3}	3.22×10^{-3}	9.56	0.74	10.0	7.90×10^{-4}	8.32×10^{-7}	0.23
	3×10^{-5}	4.50×10^{-6}	1	2	0.01	0	3.83×10^{-3}	1.19×10^{-2}	4.61	0.67	16.3	9.56×10^{-4}	1.79×10^{-6}	0.62
	3×10^{-5}	4.50×10^{-6}	1	1	0.01	0	4.28×10^{-3}	1.18×10^{-2}	3.56	0.81	16.6	1.88×10^{-3}	2.09×10^{-6}	0.58
	3×10^{-5}	9.00×10^{-6}	1	1	0.01	0	5.98×10^{-3}	1.17×10^{-2}	4.03	0.78	20.1	9.46×10^{-4}	4.20×10^{-6}	0.52
	3×10^{-5}	9.00×10^{-7}	1	2	0.05	1	4.99×10^{-3}	3.91×10^{-3}	16.0	0.66	7.0	6.94×10^{-4}	6.24×10^{-7}	0.27
	3×10^{-5}	1.80×10^{-6}	1	2	0.05	1	6.81×10^{-3}	4.24×10^{-3}	24.0	0.48	8.1	4.01×10^{-4}	1.36×10^{-6}	0.25
	3×10^{-5}	9.00×10^{-7}	1	2	0.05	0.5	3.56×10^{-3}	2.80×10^{-3}	13.7	0.63	7.8	7.31×10^{-4}	3.26×10^{-7}	0.25
	10^{-4}	6×10^{-5}	1	5	0.01	0	1.21×10^{-2}	2.24×10^{-2}	7.19	0.53	13.3	4.23×10^{-4}	2.63×10^{-5}	0.45
	10^{-4}	6×10^{-5}	1	2	0.01	0	1.20×10^{-2}	0	n/a	n/a	14.5	0	2.65×10^{-5}	0
	10^{-4}	3×10^{-5}	1	5	0.05	1	2.22×10^{-2}	1.27×10^{-2}	36.0	0.32	6.0	3.34×10^{-4}	2.59×10^{-5}	0.18
	10^{-4}	3×10^{-5}	1	5	0.05	0.5	1.32×10^{-2}	1.95×10^{-2}	9.23	0.53	8.1	6.09×10^{-4}	1.66×10^{-5}	0.38
T	10^{-4}	1.5×10^{-5}	1	10	0.05	0	5.19×10^{-3}	1.88×10^{-2}	7.17	0.49	9.2	8.17×10^{-4}	3.98×10^{-6}	0.54
C	10^{-4}	1.5×10^{-5}	1	10	0.05	1	1.20×10^{-2}	1.76×10^{-2}	13.3	0.47	7.4	3.98×10^{-4}	1.21×10^{-5}	0.32
	10^{-4}	1.5×10^{-5}	1	10	0.05	0.5	8.44×10^{-3}	1.99×10^{-2}	9.36	0.49	7.6	6.03×10^{-4}	7.59×10^{-6}	0.43
	10^{-4}	3×10^{-5}	1	2	0.05	0	8.64×10^{-3}	1.64×10^{-2}	4.66	0.62	12.6	1.51×10^{-3}	1.02×10^{-5}	0.43
	10^{-4}	3×10^{-5}	1	2	0.05	1	2.38×10^{-2}	5.63×10^{-3}	40.4	0.32	6.1	4.08×10^{-4}	2.54×10^{-5}	0.07
	10^{-4}	3×10^{-5}	1	2	0.05	0.5	1.60×10^{-2}	1.29×10^{-2}	7.93	0.68	7.1	9.56×10^{-4}	1.68×10^{-5}	0.25
	10^{-4}	6×10^{-5}	1	2	0.05	0.5	2.06×10^{-2}	1.71×10^{-2}	7.23	0.64	8.1	6.65×10^{-4}	3.56×10^{-5}	0.30
	10^{-4}	6×10^{-5}	1	2	0.05	0	1.54×10^{-2}	8.53×10^{-3}	10.4	0.53	14.1	4.63×10^{-4}	2.43×10^{-5}	0.11
	10^{-4}	6×10^{-5}	1	2	0.05	1	3.22×10^{-2}	5.93×10^{-3}	44.1	0.28	6.2	2.81×10^{-4}	5.09×10^{-5}	0.06
	10^{-4}	3×10^{-5}	1	5	0.01	0	8.36×10^{-3}	1.95×10^{-2}	6.64	0.50	11.5	6.93×10^{-4}	1.12×10^{-5}	0.49
	10^{-4}	3×10^{-5}	1	5	0.05	0	8.00×10^{-3}	1.99×10^{-2}	6.55	0.52	11.7	7.66×10^{-4}	1.02×10^{-5}	0.50
	10^{-4}	1.5×10^{-5}	1	10	0.01	0	5.33×10^{-3}	1.89×10^{-2}	7.20	0.44	9.1	7.60×10^{-4}	4.40×10^{-6}	0.53
	10^{-4}	3×10^{-5}	1	10	0.01	0	7.83×10^{-3}	2.27×10^{-2}	7.68	0.48	11.5	4.57×10^{-4}	1.13×10^{-5}	0.50
	10^{-4}	3×10^{-5}	1	10	0.05	0	7.58×10^{-3}	2.23×10^{-2}	7.39	0.48	11.9	4.80×10^{-4}	1.04×10^{-5}	0.50
	10^{-4}	3×10^{-5}	1	10	0.05	1	1.83×10^{-2}	1.90×10^{-2}	19.0	0.38	7.0	2.71×10^{-4}	2.59×10^{-5}	0.25
	10^{-4}	3×10^{-5}	1	10	0.05	0.5	1.20×10^{-2}	2.23×10^{-2}	10.2	0.50	8.8	3.99×10^{-4}	1.68×10^{-5}	0.37
	10^{-4}	4×10^{-4}	1	5	0.01	0	3.63×10^{-2}	2.40×10^{-2}	47.8	0.17	13.7	1.05×10^{-4}	2.09×10^{-4}	0.26
	10^{-4}	$\times 10^{-4}$	1	5	0.01	0	1.70×10^{-2}	2.34×10^{-2}	11.0	0.50	12.4	3.04×10^{-4}	4.65×10^{-5}	0.38
	10^{-4}	1.5×10^{-4}	1	5	0.01	0	2.26×10^{-2}	2.26×10^{-2}	19.2	0.30	11.5	2.14×10^{-4}	7.26×10^{-5}	0.32
	10^{-4}	1.5×10^{-4}	1	5	0.05	0	2.21×10^{-2}	2.05×10^{-2}	18.8	0.33	13.1	1.98×10^{-4}	6.81×10^{-5}	0.30
	10^{-4}	2.5×10^{-4}	1	5	0.01	0	2.92×10^{-2}	2.06×10^{-2}	46.9	0.18	13.5	1.28×10^{-4}	1.26×10^{-4}	0.26
	10^{-4}	$\times 10^{-4}$	1	2	0.05	0.5	2.80×10^{-2}	1.74×10^{-2}	8.31	0.54	7.6	4.72×10^{-4}	6.17×10^{-5}	0.26
	$\times 10^{-4}$	2×10^{-4}	1	2	0.05	0.5	4.14×10^{-2}	1.72×10^{-2}	18.3	0.38	7.2	2.73×10^{-4}	1.27×10^{-4}	0.18
	3×10^{-4}	1.80×10^{-5}	1	3	0.35	10	2.28×10^{-2}	3.52×10^{-3}	14.3	0.73	6.9	1.03×10^{-3}	2.96×10^{-5}	0.02
	3×10^{-4}	2.48×10^{-5}	1	3	0.35	10	2.64×10^{-2}	1.61×10^{-3}	38.1	0.49	7.2	7.75×10^{-4}	4.20×10^{-5}	0.04
	3×10^{-4}	3.15×10^{-5}	1	3	0.35	10	2.92×10^{-2}	2.30×10^{-3}	70.0	0.35	7.6	6.61×10^{-4}	5.45×10^{-5}	0.07
	3×10^{-4}	4.50×10^{-5}	1	3	0.35	10	3.34×10^{-2}	6.78×10^{-3}	60.0	0.40	8.0	5.81×10^{-4}	8.00×10^{-5}	0.04
	3×10^{-4}	7.20×10^{-5}	1	3	0.35	10	4.01×10^{-2}	1.17×10^{-2}	106.3	0.27	8.3	5.03×10^{-4}	1.31×10^{-4}	0.10
	3×10^{-4}	1.08×10^{-4}	1	3	0.35	10	4.87×10^{-2}	1.61×10^{-2}	161.7	0.22	8.4	4.44×10^{-4}	2.30×10^{-4}	0.14
	3×10^{-4}	4.50×10^{-4}	1	3	0.35	2	4.61×10^{-2}	1.59×10^{-2}	85.8	0.20	9.0	4.80×10^{-4}	2.02×10^{-4}	0.13
	3×10^{-4}	9.41×10^{-4}	1	3	0.35	1	4.82×10^{-2}	2.83×10^{-2}	20.2	0.40	10.1	5.52×10^{-4}	2.95×10^{-4}	0.24
	3×10^{-4}	1.05×10^{-3}	1	3	0.35	1	5.14×10^{-2}	2.78×10^{-2}	28.2	0.32	10.0	5.09×10^{-4}	3.29×10^{-4}	0.23

proper to this study are the following: the convective power density p is the ratio of the convective power defined in Christensen & Aubert (2006) to the shell volume $V = 4\pi(r_o^3 - r_i^3)/3$. The magnetic dissipation time τ_{diss} is defined as in Christensen & Tilgner (2004), by dividing the magnetic energy by the power dissipated through ohmic losses. However, in that study τ_{diss} was normalized by the dipole diffusion time. Here we choose to normalize this quantity by the standard magnetic diffusion time $\tau_{mag} = D^2/\lambda$, in order to account for the variation in the shell gap D throughout geological time. For the determination of the system behaviour regarding the occurrence of reversals, a standard length of three to five magnetic diffusion times was used.

2.2 Generalized relationship between convective power and mass anomaly flux/Rayleigh number

Here we derive a general relation between the convective power density p and the Rayleigh number Ra_Q. Buffett *et al.* (1996) demonstrated that under the assumption of good mixing (sufficiently supercritical convection), the total dissipation Φ of the dynamo is proportional to the sum of the inner- and outer- boundary originated mass anomaly fluxes

$$\Phi = \Phi_i + \Phi_o = F_i(\psi_i - \overline{\psi}) + F_o(\overline{\psi} - \psi_o). \quad (15)$$

Here ψ is the gravitational potential such that the gravity vector is $\mathbf{g} = -\nabla\psi$, and ψ_i, ψ_o, $\overline{\psi}$ are, respectively, the inner boundary, outer boundary, and mean values of the gravitational potential. The physical meaning of (15) is that the dissipation results from taking mass anomaly at a given gravitational potential, and redistributing it at the mean gravitational potential, which is where the good mixing assumption enters.

In the present context of radial gravity, the gravitational potential is expressed as $\psi = r^2 g_o/2r_o + cst$. The expression for $\overline{\psi}$ is (Buffett *et al.* 1996)

$$\overline{\psi} = \frac{3g_o}{10r_o}\left(\frac{r_o^5 - r_i^5}{r_o^3 - r_i^3}\right). \quad (16)$$

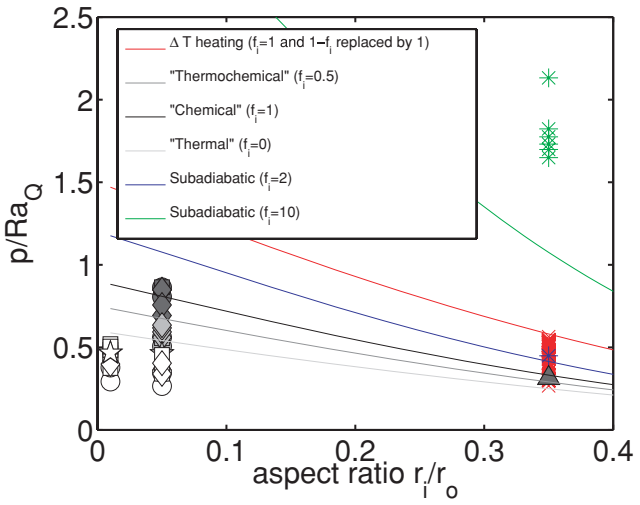

Figure 1. Test of the perfect mixing theoretical p/Ra_Q relationship with numerical data. Symbols represent the numerical data, and lines represent the theoretical prediction of eqs (18) and (17). Red colour: Christensen & Aubert (2006) data points. Our theory applies to their choice of fixed temperature boundary conditions provided f_i and $1 - f_i$ are replaced by 1 in eq. (18). White symbol filling and light grey line: cases of secular cooling with $f_i = 0$. Medium-grey symbol filling and line: cases of thermochemical convection with $f_i = 0.5$. Dark-grey symbol filling and black line: cases of purely chemical convection with $f_i = 1$. Blue symbols and lines: cases where the shell is stably stratified at the outer boundary (subadiabatic system) with $f_i = 2$. Green symbols: same as blue, for $f_i = 10$. For symbol shape definitions see Fig. 3.

Expanding (15) with the help of (16), and making use of the fact that the conservation of energy, when averaged over times long relatively to core flow timescales, yields $(\rho\Omega^3 D^2)\ pV = \Phi$ (recall that p is a dimensionless quantity), we obtain after some algebra the following proportionality relationship between the power per unit volume p and the total mass anomaly flux F

$$p = \gamma\, Ra_Q \tag{17}$$

with

$$\gamma = \frac{3(r_o - r_i)^2}{2\left(r_o^3 - r_i^3\right) r_o}\left[f_i\left(\frac{3}{5}\frac{r_o^5 - r_i^5}{r_o^3 - r_i^3} - r_i^2\right) + (1 - f_i)\left(r_o^2 - \frac{3}{5}\frac{r_o^5 - r_i^5}{r_o^3 - r_i^3}\right)\right]. \tag{18}$$

Eqs (18) and (17) are the generalizations to arbitrary buoyancy distributions of the relationships obtained in appendix A of Christensen & Aubert (2006). They are tested versus our numerical data in Fig. 1. The agreement between theoretical and numerical values of p/Ra_Q becomes good as the supercriticality of convection increases. Cases with a strong stable density stratification (i.e. $f_i \gg 1$) need a stronger level of mixing to approach the theoretical line. This is simply a consequence of the fact that convection does not fill the entire shell in these cases. For a given level of convection supercriticality, the mass anomaly, while indeed produced at the inner boundary, fails to be redistributed at the mean gravitational potential of the shell to a greater extent.

For the scaling relationships to be presented in the next section, the use of p instead of Ra_Q as a basic scaling parameter is motivated by several important reasons. First, the theory underlying these scalings (Christensen & Aubert 2006) relies on convective power arguments, while Ra_Q is merely an approximate proxy for convective power. In our present study, where we vary the buoyancy partition f_i and the aspect ratio χ, the use of Ra_Q as a basic scaling parameter does not capture the geometrical and buoyancy distribution effects contained in (18), thus resulting in a large scatter that the use of p corrects for. Another advantage of using p instead of Ra_Q is that p is a geophysical parameter which is constrained by thermodynamic studies of the Earth's core (e.g. Lister 2003, see Section 3.2). Finally, expressing the scalings with p leads to a useful internal consistency relationship to be detailed in Section 3.3.

2.3 Statistics of least-squares fits

In Section 3.1, we obtain power laws of the form $y = ax^b$ from numerical data. The problem reduces to getting a linear least squares fit of the form $\ln y = \ln a + b \ln x$. In this fit, the slope b is usually fairly well constrained by the large number of data points available. The standard least-squares error σ_b on b is therefore discussed only as we check the internal consistency of the scalings. For all other purposes, the vertical variance σ^2 of the errors $e_i = \ln \hat{y}_i - \ln y_i$ is used, and as a standard practice, we present the best-fitting laws $y = ax^b$ together with their 3σ lines $y = (a/e^{3\sigma})x^b$ and $y = ae^{3\sigma}$ x^b, which theoretically enclose 99.7 per cent of the data if the distribution of errors e_i is normal.

3 RESULTS

3.1 Results from numerical dynamos

We first present (Fig. 2) images from two models with a small inner core ($\chi = 0.05$, see Table 1 for other parameters). Model C is driven by inner-boundary originated buoyancy (chemical convection, $f_i = 1$), and model T is driven by volumetric heating and outer-boundary originated buoyancy (secular cooling, $f_i = 0$). Convection sets up where the thermochemical gradients are most unstable: one single convection cell near the inner boundary for C, five cells extending from mid-shell to the outer boundary for T. DMFI visualization (Aubert *et al.* 2008) reveals that the magnetic field is generated according to the classical macroscopic α^2 mechanism (Olson *et al.* 1999), although model C additionally has an enhanced toroidal field production by zonal flow near the outer boundary. Both models are dipole-dominated, with magnetic dipoles of similar relative strengths (C and T, respectively, have $f_{dip} = 0.47, 0.49$). They are typically less dipolar than similar models with $\chi = 0.35$ (see Fig. 6). In model T, the lower dipolarity can be explained by shallow convection columns which enhance magnetic flux expulsion and thus enrich the outer boundary power spectrum in multipolar content. In model C, the small inner core surface over which the buoyancy is distributed favours the occurrence of magnetic upwellings (Aubert *et al.* 2008) which reduce the dipolarity by frequently disrupting the magnetic dipole. In both models, the absence of the inner core favours a global axisymmetric poloidal circulation, which, at a given instant in time, concentrates magnetic field at one pole and disperses it at the other pole (in the snapshots presented in Fig. 2, flux concentration is occurring at the south pole for model C and the north pole for model T). It should finally be noted that in thermal models, the absence of buoyancy at the inner-core boundary decouples the inner core from the convection and dynamo processes, with two consequences: first, thermal models with $\chi = 0.05$ or 0.01 yield almost the same results, which are presumably those which would be obtained from a case where $r_i = 0$. Second, the relationship

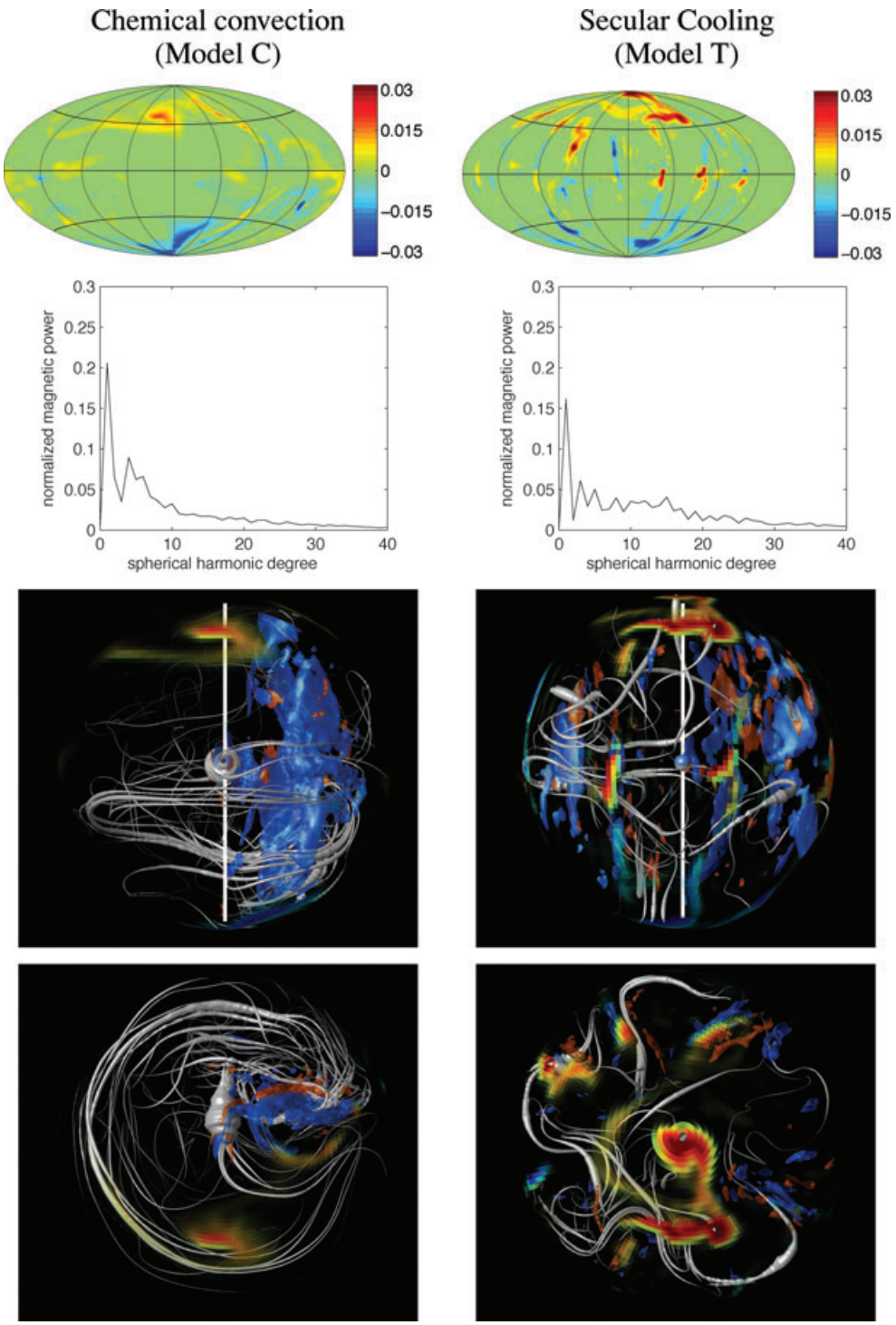

Figure 2. Magnetic field and flow morphologies from a chemically driven model (C, $f_i = 1$), and a model driven by secular cooling (T, $f_i = 0$). See Table 1 for other parameters. From top to bottom: Hammer projections of the radial magnetic field at the outer boundary, harmonic degree power spectra normalized by the total power, DMFI equatorial and polar visualizations. The DMFI images present magnetic field tubes (grey) with thicknesses normalized by the local magnetic energies, as well as two isosurfaces of the axial vorticity $\omega_z = (\nabla \times \mathbf{u}) \cdot \mathbf{e}_z$, with levels -0.54 (blue) and 0.54 (red) for model C, and ± 0.18 for T. The outer boundary is colour coded with the radial magnetic field, with similar colour scheme as on the Hammer projections. The thick white line is the rotation axis. For other details on DMFI imaging see Aubert *et al.* (2008).

between reverse magnetic flux patch locations and inner core size (Stanley *et al.* 2007) does not hold if secular cooling drives the dynamo.

Fig. 3 presents a plot of the Rossby number *Ro* (or dimensionless rms flow velocity) versus the dimensionless convective power *p*. The best fit and 3σ lines have equations

$$Ro = (0.69, 1.31, 2.49)p^{0.42}. \quad (19)$$

When cast into a $p - Ro$ space, the Christensen & Aubert (2006) scaling is virtually unchanged by the addition of the new data points

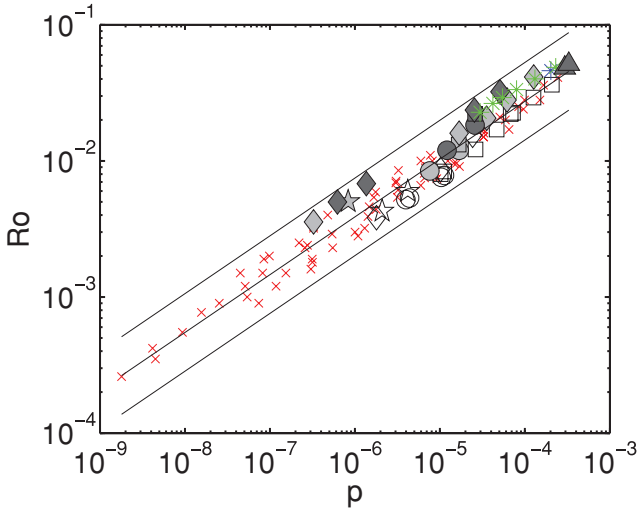

Figure 3. Dimensionless rms velocity, or Rossby number Ro as a function of the dimensionless convective power p. Red crosses are the Christensen & Aubert (2006) data points. Other symbol colours are defined in Fig. 1. Symbol shapes are as follows: small aspect ratio models ($\chi < 0.05$) have circles for $Pm = 10$, squares for $Pm = 5$, diamonds for $Pm = 2$, filled stars for $Pm = 1$. Present aspect ratio ($\chi = 0.35$) additional models (triangles and open stars) have $Pm = 3$. Our data set is filtered to exclude the non-dynamo run.

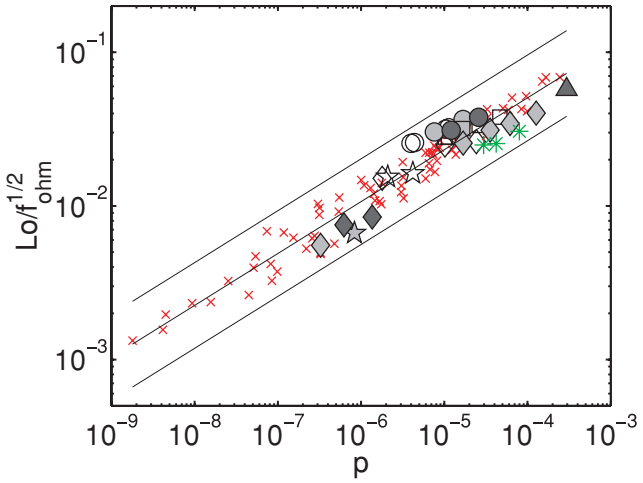

Figure 4. Dimensionless magnetic field, or Lorentz number Lo, corrected with the ohmic dissipation fraction $f_{\rm ohm}^{0.5}$, as a function of the dimensionless convective power p. Symbols as in Fig. 3. Our data set is filtered to exclude dynamos with a dipole fraction $f_{\rm dip} \leq 0.35$.

with variable inner core size and buoyancy distribution, with a scatter which is also unchanged. In the dipole-dominated regime ($f_{\rm dip} > 0.35$), the same remarks hold for the Lorentz number Lo (or dimensionless rms magnetic field) scaling (Fig. 4), which obeys

$$Lo/f_{\rm ohm}^{0.5} = (0.62, 1.17, 2.22)p^{0.34}. \tag{20}$$

We deduce that the convective power p is the primary scaling parameter for magnetic and velocity field amplitude, and integrates the relevant dependencies on inner core size and buoyancy distributions for our present purposes. We further check (Fig. 5) the relation between the magnetic dissipation time $\tau_{\rm diss}$ and the magnetic Reynolds number $Rm = RoPm/E$ (Christensen & Tilgner 2004)

$$\tau_{\rm diss}/\tau_{\rm mag} = (0.11, 0.26, 0.65)Rm^{-1.0}. \tag{21}$$

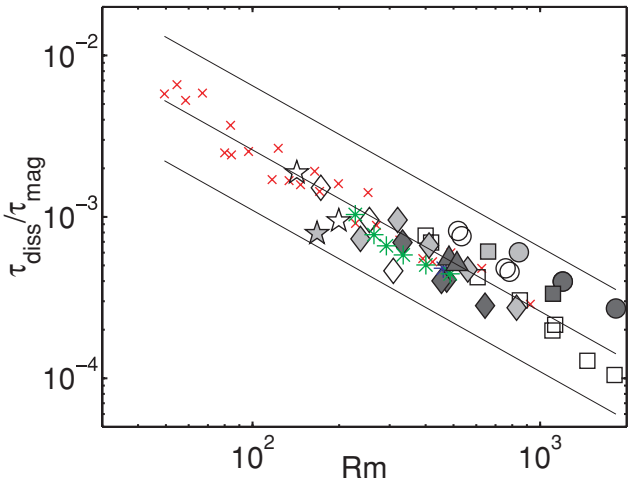

Figure 5. Magnetic dissipation time $\tau_{\rm diss}$, normalized by the standard magnetic diffusion time $\tau_{\rm mag}$, as a function of the magnetic Reynolds number Rm. Symbols as in Fig. 3, except the red crosses which represent the Christensen & Tilgner (2004) models. Our data set is filtered to exclude the non-dynamo run.

For this last scaling, the newer runs cause a significantly larger scatter than that obtained by Christensen & Tilgner (2004). We attribute this to the rather small size (26 models) and limited parameter space extent of the data set used in that study, and conclude that the aspect ratio and buoyancy distribution have little influence on this scaling.

For an extrapolation of the three scalings presented above to Earth's core conditions, the scaling prefactors need to be determined. Here we derive a useful internal consistency relationship tying these prefactors. We first define the dimensional values $B_{\rm rms}$ and $U_{\rm rms}$ for Lo and Ro, expand them using (19) and (20) and also recall the definition of $\tau_{\rm diss}$

$$B_{\rm rms} = Lo(\rho\mu)^{1/2}\Omega D = c_1 f_{\rm ohm}^{0.5} p^{0.34}(\rho\mu)^{1/2}\Omega D, \tag{22}$$

$$\tau_{\rm diss} = c_2 Rm^{-1} D^2/\lambda \text{ with } Rm = U_{\rm rms} D/\lambda \tag{23}$$

$$U_{\rm rms} = (\Omega D)Ro = c_3 p^{0.42}\Omega D. \tag{24}$$

Here the $c_{\rm i}$ coefficients are scaling prefactors, to be chosen within the 3σ range of each scaling. In the case of the geodynamo, where the magnetic diffusivity is much larger than the viscous diffusivity, and the magnetic energy much larger than the kinetic energy, we expect most of the convective power $\rho\Omega^3 D^2 pV$ to be dissipated through ohmic losses (i.e. $f_{\rm ohm} \approx 1$), hence

$$\rho\Omega^3 D^2 p = \frac{B_{\rm rms}^2}{2\mu}\frac{1}{\tau_{\rm diss}}. \tag{25}$$

After expanding all quantities with the use of their scaling laws, the dimensionless version of (25) writes

$$1 = \frac{c_1^2 c_3}{2c_2} p^{0.1}. \tag{26}$$

This reveals a good consistency of the scalings: for instance, the dependency in λ vanishes as it should, thanks to the scaling exponent -1 in (23). However consistency is not perfect, as witnessed by the residual power 0.1 at which p appears. As in the next section, p will be assumed to vary over geological time, this will prevent (26) to be exactly satisfied with time-independent values for c_{1-3}. This problem can be related to the standard error in the least-squares determination of each exponent. We obtained standard exponent

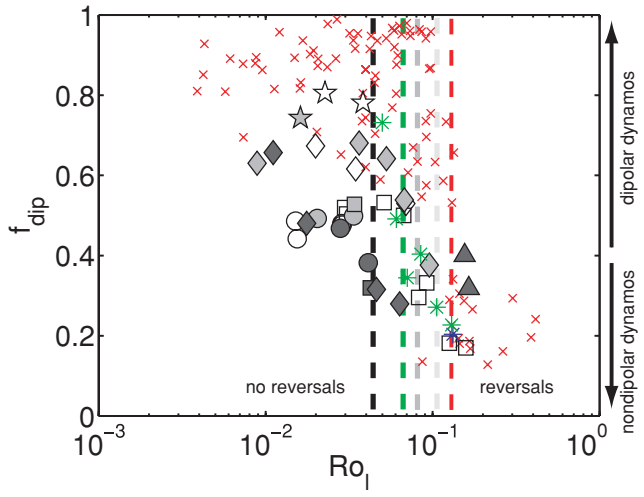

Figure 6. Dipolar fraction $f_{\rm dip}$ as a function of the local Rossby number $Ro_l = Ro\bar{l}/\pi$. Symbols as in Fig. 3. The dashed lines delineate the transition point from stable to reversing dynamos: red dashes for the $\chi = 0.35$ models from Christensen & Aubert (2006), green for $\chi = 0.35$ and $f_{\rm i} > 1$, light grey for $\chi = 0.01$–0.05 and $f_{\rm i} = 0$, medium grey for $\chi = 0.01$–0.05 and $f_{\rm i} = 0.5$, black for $\chi = 0.01$–0.05 and $f_{\rm i} = 1$. Our data set is filtered to exclude the non-dynamo run.

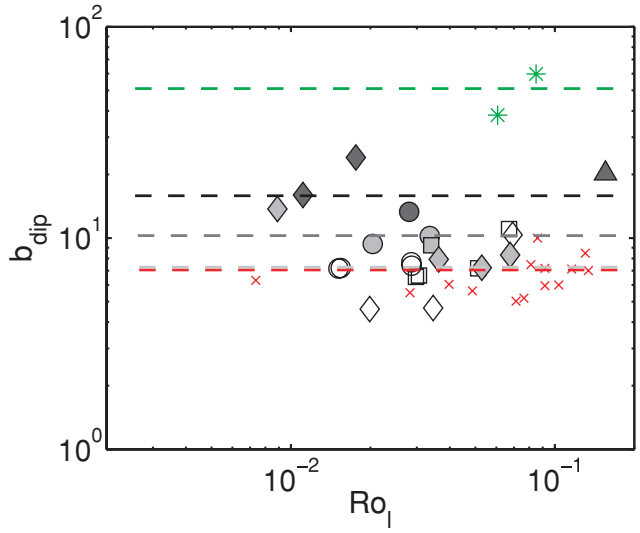

Figure 7. Ratio $b_{\rm dip}$ of the rms magnetic field inside the shell to the dipole field at the outer boundary, as a function of the local Rossby number Ro_l. Symbols as in Fig. 3. The dashed lines locate the predictions of model (28), with same colour conventions as in Fig. 6. Our data set is filtered to retain dynamos with a dipole fraction $0.4 < f_{\rm dip} < 0.7$.

errors of $\sigma_{b1} = 0.0169$, $\sigma_{b2} = 0.0639$ and $\sigma_{b3} = 0.0178$ for the Lo, $\tau_{\rm diss}$ and Ro scalings, respectively. The error on the exponent of the ohmic dissipation, in the right-hand side of (26), is therefore

$$\sigma_b = 2\sigma_{b1} + 0.42\sigma_{b2} + \sigma_{b3} = 0.078. \quad (27)$$

As σ_b is comparable with the residual power 0.1 present in (26), we conclude that this inconsistency reflects the inherent error introduced by data scatter in the least-squares fitting procedure used to derive the three scalings. This error remains small however, and can be compensated (as will be done in Section 3.3) by choosing a set of c_{1-3} that minimizes the deviations caused by $p^{0.1}$ (typically 20 per cent).

The control parameter $Ro_l = Ro\bar{l}/\pi$ was identified in Christensen & Aubert (2006) as the main parameter governing the dipolarity and stability versus reversals of numerical dynamo models. Here we follow the same approach (Fig. 6). In the dipole-dominated regime ($f_{\rm dip} > 0.35$), Fig. 6 shows again that the absence of the inner core generally decreases the dipolarity, as already explained in Fig. 2. In contrast, the influence of buoyancy distribution on dipolarity is not clear-cut and not monotonic. The critical Rossby number for reversals Ro_{lc} is located in a narrow range $Ro_{lc} = 0.04$–0.12. The frequency of polarity reversals increases with increasing departures of Ro_l from Ro_{lc}.

We then analyse (Fig. 7) the ratio $b_{\rm dip}$, which determines the relative strength of the internal field and the dipole field at the outer boundary. Since, as shown by Fig. 6, the geodynamo is likely to have had a dipolarity lower or equal to the present-day value throughout its history, we restrict the data to the range $0.4 < f_{\rm dip} < 0.7$. In this range, we find little variability of $b_{\rm dip}$ with the convective power (or Ro_l), whereas the main source of variability comes from $f_{\rm i}$ and χ. This can be attributed to depth variations of the dynamo region, the dipole seen at the surface being reduced in the case of a deeper dynamo. Indeed chemical models (deeper dynamos) have a markedly larger $b_{\rm dip}$ value than thermal models (shallow dynamos, see Fig. 2). The highest $b_{\rm dip}$ values are obtained for models with $f_{\rm i} > 1$, where the extent of the dynamo region is restricted even further by a stably stratified layer at the top of the shell (see for instance, Christensen 2006). In Section 3.3, a model will be needed for $b_{\rm dip}$ in order to estimate the dipole moment at any point in the geological history. We adopt the simplest possible linear dependency

$$b_{\rm dip} = 7.3(1-\chi)(1+f_{\rm i}). \quad (28)$$

The last scaling which we check (Fig. 8) is the relationship (Olson & Christensen 2006) between the local Rossby number Ro_l and the dynamo control parameters p, Ek, Pm and Pr. As there does not currently exist a physical rationale to exclude some control parameters, the powers in this last scaling were obtained by an approach of empirical scatter minimization. We confirm (Fig. 8a) the scaling relationship obtained by Olson & Christensen (2006)

$$Ro_l = (0.34, 0.68, 1.35) p^{0.48} E^{-0.32} Pr^{0.19} Pm^{-0.19}. \quad (29)$$

Unlike in the previous scalings, there appears an additional dependence on the aspect ratio χ, which we resolve by adopting the following relationship, yielding a smaller data scatter (Fig. 8b):

$$\frac{Ro_l}{(1+\chi)} = (0.33, 0.54, 0.89) p^{0.48} E^{-0.32} Pr^{0.19} Pm^{-0.19}. \quad (30)$$

Note that factoring out a $(1+\chi)$ dependence also slightly reduces the scatter in the critical Ro_{lc} values obtained from Fig. 6. We therefore subsequently replace the criterion for reversals $Ro_{lc} =$ 0.04–0.12 with

$$\frac{Ro_{lc}}{(1+\chi)} = (0.33, 0.54, 0.89) p^{0.48} E^{-0.32} Pr^{0.19} Pm^{-0.19} \approx 0.04\text{–}0.1. \quad (31)$$

The aspect ratio thus disappears from our condition for the onset of reversals.

3.2 Core thermodynamics and cooling models

The previous section shows how time-average properties of the past geodynamo can be estimated from the convective power. The assumed time scale for this time average is long (say a million years) compared to core flow timescales, but short compared to any geological evolution timescale of the Earth. The geological evolution

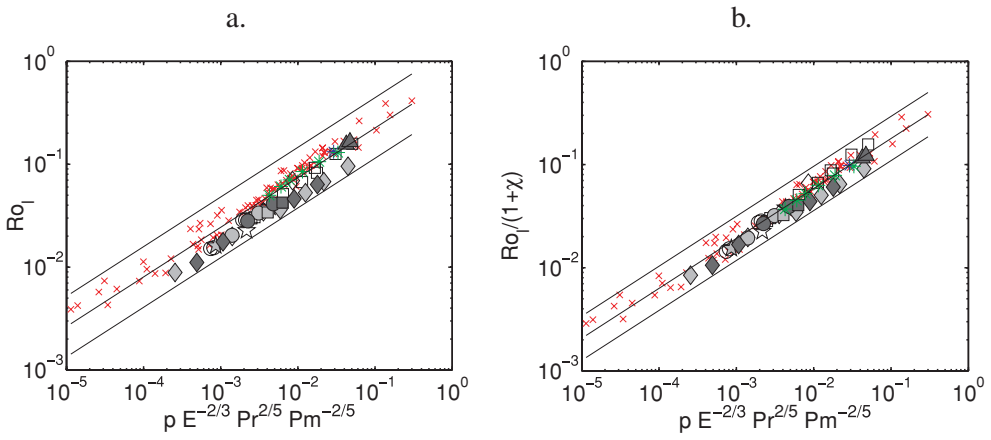

Figure 8. Local Rossby number Ro_l as a function of the combination $pE^{-2/3}Pr^{2/5}Pm^{-2/5}$ proposed in Olson & Christensen (2006). (a) Without a dependence in χ, (b) with a dependence in χ. Symbols as in Fig. 3. Our data set is filtered to exclude the non-dynamo run.

of dynamo properties can be obtained from our scaling laws if we have a long-term evolution model for the convective power, which we now derive from core thermodynamics (see the recent studies from Labrosse 2003; Lister 2003, and references therein). The fundamental inputs which are needed is an history of core-mantle heat flow $Q_{\rm cmb}(t)$, of the radioactive core heating $Q_r(t)$ and the heat flow down the isentropic temperature gradient at the CMB Q_a (hereafter termed adiabatic heat flow), which is assumed constant over time. In what follows, we use the simple parametrization of Lister (2003) which holds if the inner core volume is small relative to the outer core volume ($\chi^3 \ll 1$).

The entropy budget of the system, when time-averaged over timescales much longer than core flow timescales, but shorter than geological timescales, gives an expression for the total dynamo dissipation Φ as a function of the fundamental inputs listed above. The part $\Phi_{\rm i}$ of the dissipation that originates from mass anomaly flux at the inner boundary is then

$$\Phi_{\rm i} = (Q_{\rm cmb} - Q_r)(\epsilon_L + \epsilon_B), \tag{32}$$

where ϵ_L and ϵ_B are, respectively, the thermodynamic efficiencies of latent heat and light element release, which are given by

$$\epsilon_L = \frac{3\mathcal{L}[1-\overline{e}(\phi)]\chi}{2+3(\mathcal{L}+\mathcal{B}-\mathcal{C})\chi} \tag{33}$$

$$\epsilon_B = \frac{3\mathcal{B}\chi}{2+3(\mathcal{L}+\mathcal{B}-\mathcal{C})\chi}. \tag{34}$$

The values of the thermodynamic parameters $\mathcal{L}, \mathcal{B}, \mathcal{C}, \overline{e}(\phi)$ and ϕ are given in Table 2. The part $\Phi_{\rm o}$ of the dissipation that originates from mass anomaly flux at the outer boundary is

$$\Phi_{\rm o} = (Q_{\rm cmb} - Q_a)\epsilon_S, \tag{35}$$

where ϵ_S is the thermodynamic efficiency of thermal convection, given by

$$\epsilon_S = e^{\phi}\overline{e}(\phi) - 1. \tag{36}$$

The dimensionless, total volumetric power p can be obtained through the time average conservation of energy $\rho\Omega^3 D^2 pV = \Phi_{\rm i} + \Phi_{\rm o}$, where V is the shell volume. Once the dissipations $\Phi_{\rm i}$ and $\Phi_{\rm o}$ are known, the associated mass anomaly fluxes $F_{\rm i}$ and $F_{\rm o}$ can be retrieved from eq. (15), to finally determine $f_{\rm i} = F_{\rm i}/(F_{\rm i} + F_{\rm o})$. Note that for strongly subadiabatic cases, eq. (15) may

Table 2. Parameters used in the thermodynamic, core cooling (Section 3.2, upper panel), and palaeomagnetic (Section 3.3, lower panel) models.

Parameter	Meaning	Value	Reference
$Q_{\rm CMB}(t)$	Earth's cooling model	Variable	See Section 3.2
Q_a	Adiabatic heat flow at the CMB	6 TW	See Section 3.2
Q_r	Radiogenic heating in the outer core	0 W	See Section 3.2
$\mathcal{M}$	Heat capacity for solidification	9.2×10^{29} J	Lister (2003)
$\mathcal{L}$	Latent heat effect	2.1	Lister (2003)
$\mathcal{B}$	Buoyancy effect	0.86	Lister (2003)
$\mathcal{C}$	Compositional effect	-0.8	Lister (2003)
ϕ	Adiabatic decay parameter	0.256	Lister (2003)
$\overline{e}(\phi)$	Adiabatic decay integral	0.8595	Lister (2003)
$r_{\rm o}$	Outer core radius	3480 km	
$\Omega\,(t)$	Earth's rotation rate	variable	See Section 3.3
λ	Outer core magnetic diffusivity	$1.3\,{\rm m^2\,s^{-1}}$	Secco & Shloessin (1989)
ν	Outer core viscosity	$10^{-6}\,{\rm m^2\,s}$	de Wijs *et al.* (1998)
κ	Outer core thermochemical diffusivity (assumed to be the same as thermal diffusivity)	$5 \times 10^{-6}\,{\rm m^2\,s^{-1}}$	Stacey & Loper (2007), Labrosse *et al.* (2007), Lay *et al.* (2008)
ρ	Outer core density	$10^4\,{\rm kg\,m^{-3}}$	Dziewonski & Anderson (1981)

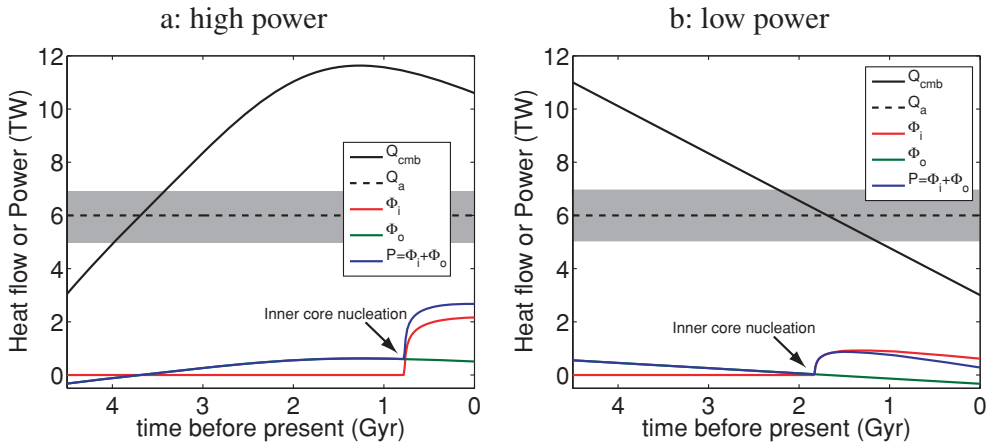

Figure 9. High- (a) and Low- (b) power models for: heat flow from the core to the mantle $Q_{\rm cmb}$, adiabatic heat flow Q_a, inner- and outer- boundary originated dissipations $\Phi_{\rm i}$, $\Phi_{\rm o}$, and total power $P = \Phi_{\rm i} + \Phi_{\rm o}$ as functions of the time before present. The greyed area represents the uncertainty range for the adiabatic heat flow. The inner core nucleates at $a \approx 1.8$ Ga before present in the low power scenario, and $a \approx 0.8$ Ga before present in the high-power scenario.

not hold because of incomplete mixing, which in this case might lead to an underestimation of $F_{\rm i}$. It should be mentioned here that breaking the total dissipation Φ into boundary-originated terms, and equating these two terms separately to their equivalent convective fluxes is not a trivial operation, since dissipation is a global non-linear quantity. The derivation presented in appendix shows that this is legitimate if the accuracy of the Boussinesq approximation is tolerable.

Once the inner core is present, the evolution of the inner core aspect ratio χ is constrained by the heat capacity for solidification $\mathcal{M}$ (value in Table 2) through the equation

$$\mathcal{M}\frac{\rm d}{{\rm d}t}\left[\chi^2 + (\mathcal{L} + \mathcal{B} - \mathcal{C})\chi^3\right] = -(Q_{\rm cmb} - Q_r). \qquad (37)$$

Eq. (37) can be integrated backwards in time from present (Labrosse *et al.* 2001) until the inner core age a (Here time is measured before present, therefore $a > 0$).

The amount of radioactive heating Q_r in planetary cores is debated. Experiments of potassium partitioning between iron and silicates suggest that present maximum potassium concentration amounts to values ranging from 30 p.p.m (Hirao *et al.* 2006) to 60–130 p.p.m (Rama Murthy *et al.* 2003), the maximum value being obtained for a sulphur rich (10 per cent wt.) core, which is not favoured for the Earth based on geochemical constraints (McDonough 2003) yielding a sulphur content of 3 per cent wt. An upper bound of 60 p.p.m for the Earth's core seems therefore reasonable and contributes 0.4 TW of present radioactive power, which is quite low when compared to typical $Q_{\rm cmb}$ values. Radioactivity was obviously stronger in the past (in the case of potassium, the power is double every 1.26 Gyr backwards), but this would amount to typically 1.5 TW at 3 Ga ago, which again is quite low compared to estimated $Q_{\rm cmb}$ at that time. In the present study, we therefore neglect the radioactive heating throughout the Earth's history, that is, $Q_r = 0$. Its inclusion is straightforward but unnecessary at this point.

The value of the adiabatic heat flow Q_a is uncertain and debated. Following Stacey & Loper (2007), Labrosse *et al.* (2007) and Lay *et al.* (2008), we adopt $Q_a = 6$ TW for a central value and allow for an uncertainty range of 1 TW above and below this value. This would correspond to a central value of the upper outer core thermal conductivity of about 50 W m^{-1} K at the top of the core (Labrosse 2003).

We now turn to the central unknown of our analysis, the history of the heat flow at the CMB, $Q_{\rm cmb}(t)$. Since there are many uncertainties involved in the determination of Earth cooling models, as well as in our present modelling effort, our goal is not to propose a definitive model for the geologic evolution of the geodynamo, which would be based on a definitive model for $Q_{\rm cmb}(t)$. Rather, we focus on two end-member scenarios representing the variety of geophysical situations which can be expected based on the uncertainties (Fig. 9). The first one, which we label as the high-power scenario, was proposed by Labrosse *et al.* (2007). It is motivated by the large (about 10 TW) present heat flows at the CMB deduced from post-perovskite seismological studies (Hernlund *et al.* 2005; Lay *et al.* 2006), from geochemical constraints and from the suggested present crystallization of a basal magma ocean in the lower mantle. As indicated by Fig. 9(a), it yields a typical dynamo power of 2.7 TW at present. The second, low power scenario is motivated by the fact that the scaling of ohmic dissipation in numerical dynamos (Christensen & Tilgner 2004) favours a low present dissipation of about 0.2–0.5 TW. Using the thermodynamic analysis presented above, this implies that the top of the Earth's core is presently sub-adiabatic ($Q_{\rm cmb} < Q_a$, see Fig. 9b). A variety of idealized, constant rate cooling histories can be built, which cross the adiabat at an age b. Plausible models are such that $b \leq a$ (Labrosse *et al.* 1997), because if $b > a$ then convection stops in the Earth's core between the adiabat crossing and the nucleation of the inner core. This is not acceptable since a conducting core would not cool fast enough to subsequently nucleate an inner core before present. Our second scenario is built according to this constraint, taking an initial CMB heat flow of $Q_{\rm cmb} = 11$ TW, and a present value $Q_{\rm cmb} = 3$ TW, corresponding to a present dynamo power of about 0.3 TW.

3.3 Time evolution models for palaeomagnetic observables

We now combine the dynamo scaling study from Section 3.1 with the thermodynamic elements from Section 3.2 in order to evaluate how the main properties of the geodynamo evolve over time. At any point in time, the power p can be accessed from the analysis of the previous section. The Prandtl and magnetic Prandtl numbers are set according to the diffusivity values listed in Table 2. In order to determine the Ekman number E, the rotation rate of the Earth is needed. We use the length-of-day model (LOD) of Varga

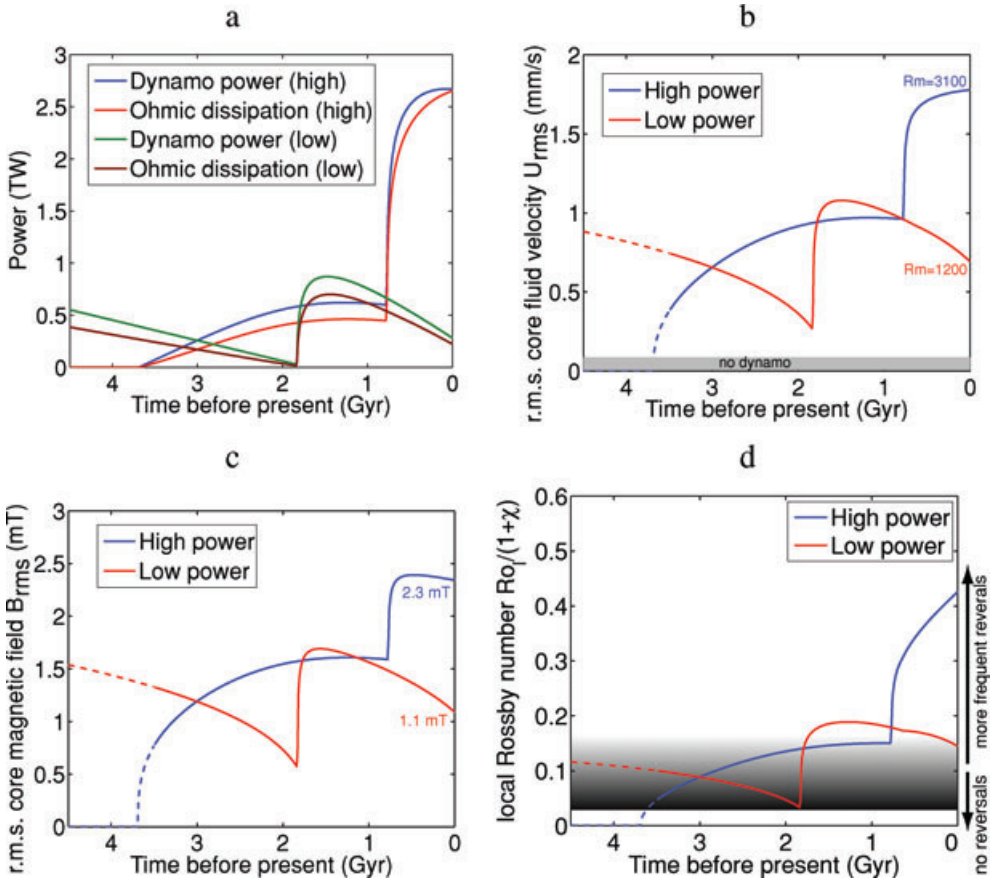

Figure 10. (a) Dynamo power and ohmic dissipation (respectively, left- and right-hand side of the internal consistency relationship (25), both multiplied by the shell volume V), using the prefactor set $(c_1, c_2, c_3) = (1.65, 0.11, 1.31)$ for both scenarios. (b) rms core velocity $U_{\rm rms}$, with indications of the equivalent magnetic Reynolds numbers Rm at present, and a rough delineation of the dynamo onset which would correspond to $Rm \approx 40$ (Christensen & Aubert 2006). (c) rms core magnetic field $B_{\rm rms}$. (d) Local magnetic Reynolds number Ro_l (corrected by $1 + \chi$). For this last scaling the central value 0.54 from (30) is used, and the 3σ uncertainty range is propagated to the location of the critical value Ro_{lc} for reversals obtained from (31) (shaded zone, lighter shade of grey means higher likeliness for reversals/higher reversal frequency). In (b)–(d), the dashes represent the epoch with no available palaeomagnetic samples.

et al. (1998), according to which the LOD has piecewise linearly increased from 19 hr 2.5 Ga ago to 20.8 hr 0.64 Ga ago, and to 24 hr today. As there is no constraint on earlier length of day, we backward continue the 2.5–0.5 Ga trend, thus yielding an initial length of day of 17 hr. It should be mentioned that the length-of-day variation should not exceed a factor 2 in any case, which has a weak impact on the scalings where the Ekman number is present.

The determination of absolute values for dynamo properties is subject to a considerable amount of uncertainty, which is discussed in detail in the next section. For that reason, we focus on the trends, or absence thereof, rather than the absolute values. Here we therefore present time evolution models obtained with scaling prefactors from (22) and (24) as close to their central values as possible, while still satisfying the constraint (26) of internal consistency. Using the central values for the prefactors $c_{\rm i}$ as a starting point, we obtain $p^{0.1}c_1^2c_3/2c_2 \approx 0.2$ throughout time. We therefore need to adjust the prefactors $c_{\rm i}$ within the 3σ error range, increasing $c_{1,3}$ and decreasing c_2. In order to keep $c_{1,3}$ close to their central values, we first decrease c_2 from 0.26 to its minimal acceptable value 0.11. There subsequently remains some discrepancy in (26), which we cancel out by increasing c_1 from 1.17 to 1.65 while keeping $c_3 = 1.31$. Our predictions for $U_{\rm rms}$ (or the magnetic Reynolds number Rm), $B_{\rm rms}$ and the local Rossby number Ro_l are reported in Figs 10(b), (c) and (d). We note that the model for $B_{\rm rms}$ implicitly assumes that $f_{\rm ohm} \approx 1$ throughout time, and that the dynamo has been dipole-dominated throughout Earth's history. This last point is reasonable since our models show that Ro_l, the parameter controlling the breakdown of dipolarity (Fig. 6) has been below its present-day value throughout Earth's history (Fig. 10d).

An illustrative indication of how the internal properties evolution previously computed may translate to surface observables can be obtained by computing the true dipole moment

$$M = \frac{4\pi r_{\rm o}^3}{\sqrt{2}\mu}\frac{B_{\rm rms}}{b_{\rm dip}}. \tag{38}$$

For the determination of $b_{\rm dip}$, we use the simple model (28), the time evolution of which is presented in Fig. 11(a). In order to put the results in perspective with the considerable scatter in palaeointensity data, the resulting true dipole moment time-series (Fig. 11b) are presented together with virtual dipole moment values (VDM) from the IAGA palaeointensity database (Perrin & Schnepp 2004; Biggin *et al.* 2009).

4 DISCUSSION

Fig. 11(b) shows that throughout the Earth's history, the dipole moments predicted by our models agrees with the observed palaeointensities to better than an order of magnitude, a fact which can be

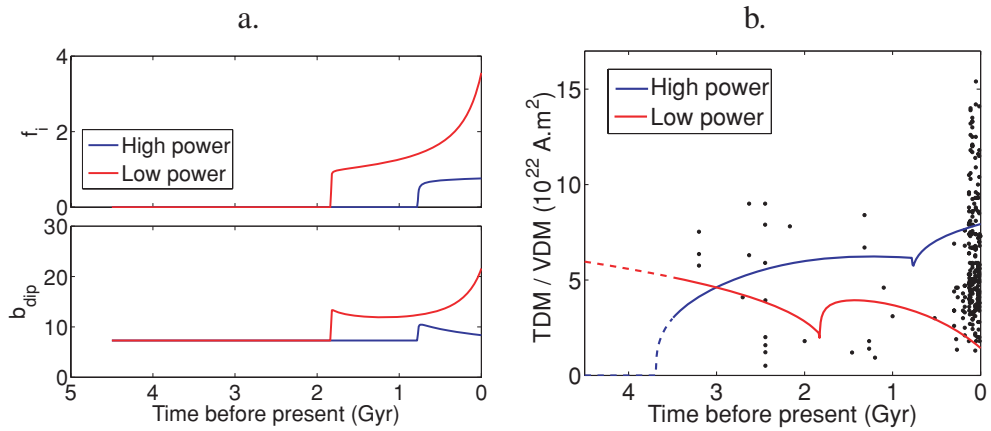

Figure 11. (a) Time evolutions for f_i, obtained from (15), and for b_{dip}, obtained from (28). (b) Time evolution models for the true dipole moment (TDM) M, with the same choice of scaling prefactors as in Fig. 10. The black dots represent the virtual dipole moment (VDM) values from the IAGA palaeomagnetic database (Perrin & Schnepp 2004; Biggin *et al.* 2009). Only VDM data obtained from Thellier–Thellier-type experiments using pTRM consistency checks (Thellier & Thellier 1959) were selected for robustness. Samples with an age of less than 10 Myr, of unknown or transitional polarity, or with VDM standard deviation greater than 20 per cent of the mean were also excluded, thus reducing the data set to 224 reliable points, 24 of which corresponding to the Precambrian.

seen as a success for the underlying theories of convective dynamos and core thermodynamics. However, it must be kept in mind that a more specific analysis, such as discriminating between the high- and low-power scenarios based on comparison with palaeointensity data, is necessarily plagued by a considerable amount of uncertainty. First, we have used central prefactor values for our scaling predictions, bearing a typical uncertainty of a factor 2 above and below the central line. Similarly, the conversion from deep to surface properties is also suffering from a similar factor 2 uncertainty (Fig. 7) and from departures from the perfect mixing theory (though in our models, f_i does not greatly exceed 1, thus limiting the impact of incomplete mixing). The determination of thermodynamic properties in the upper part of Table 2 is also uncertain to a typical factor 2 (Lister 2003), which mainly affects the determination of p from a given cooling scenario. The diffusivities in the lower part of Table 2 are even less precisely determined, but we note that most of our scalings draw their interest from the fact that they are diffusivity-independent. Finally, the palaeointensity data against which we compare our models has a large scatter which could result from either time variability of the field or intrinsic determination uncertainty (Tauxe & Yamazaki 2007). In these respects, the most significant conclusion that can be drawn from the use of the two end-member cooling scenarios is an evaluation of the sensitivity of predicted palaeointensities to uncertainties in the Earth's cooling history.

Studying the time variations of dynamo properties, rather than their absolute values, makes however more sense because among all the uncertainties listed above, a number can be supposed to be time-independent: material and thermodynamic properties, and diffusivities which are the main source of scatter around the central line in dynamo scalings. We additionally focus on trends, which are independent on the chosen cooling scenario. Still, the dipole moment variations predicted by our models are in any case small, owing to the relatively small exponent 1/3 to which the power enters in the magnetic field scaling, and smaller than the typical scatter in palaeointensity data, a fact which rationalizes the observed lack of strong long-term trends (Tauxe & Yamazaki 2007) in the palaeointensity time-series.

The outstanding events in the evolution of the internal field amplitude, as presented in Fig. 10(c), are the onset of dynamo action, and the nucleation of the inner core. Fig. 10(b) shows that the dynamo has operated above the typical value of the critical magnetic Reynolds number $Rm_c \approx 40$ (Christensen & Aubert 2006) throughout the period 3.2 Ga to present which is documented by palaeomagnetic records. Our simulations show that prior to the nucleation of the inner core, a thermal dynamo driven by secular cooling alone, and without any need for radioactivity, has no difficulties to generate a magnetic field with strength comparable to that of the present field: both cooling scenarios predict a dipole moment of 5×10^{22} A m^2 3 Ga ago, on par with present-day values, and compatible with the findings of Tarduno *et al.* (2007). Based on this result, the suggestion (Dunlop 2007) that old palaeomagnetic samples such as those analysed by Tarduno *et al.* (2007) provide evidence that the inner core was already present before 3.2 Ga ago should be discarded. While the inner-core nucleation itself certainly has a significant impact on the internal magnetic field amplitude, the signature is largely attenuated in the dipole moment time-series (Fig. 11a), due to the evolution of the conversion factor b_{dip}. Indeed, as the inner core nucleates, the onset of chemical convection brings additional thermodynamic efficiency in the system, extracting more power from a given CMB heat flow. At the same time, however, the location of the dynamo shifts from mid-shell to the shell centre, thus masking the field amplitude increase seen from the surface. The prospect of observing the signature of inner core nucleation through a sudden increase of the palaeointensity at the surface of the Earth, following the suggestion of Hale (1987), is therefore reduced.

We now discuss the predicted evolution for the dipolarity and stability of the geodynamo. Our results suggest that for a given convective forcing (more precisely, for a given local Rossby number), the absence of an inner core reduces the dipolarity. All forcing conditions being equal, the earlier geodynamo could therefore have been less dipolar than at present. However, inferring the dipolarity of the past geodynamo implies to weigh the effects of the geometry at given forcing, and of the forcing variations, a smaller Ro_l implying a possibly more stable and more dipolar dynamo (see Fig. 6). As, in both models, Ro_l has been generally lower than its present value throughout Earth's history, and also less than an order of magnitude away from the critical value Ro_{lc} for reversals (Fig. 10d), it is possible that 3–2.5 Ga ago, the effects related to the absence of the inner core and to a lower Ro_l might have compensated to yield

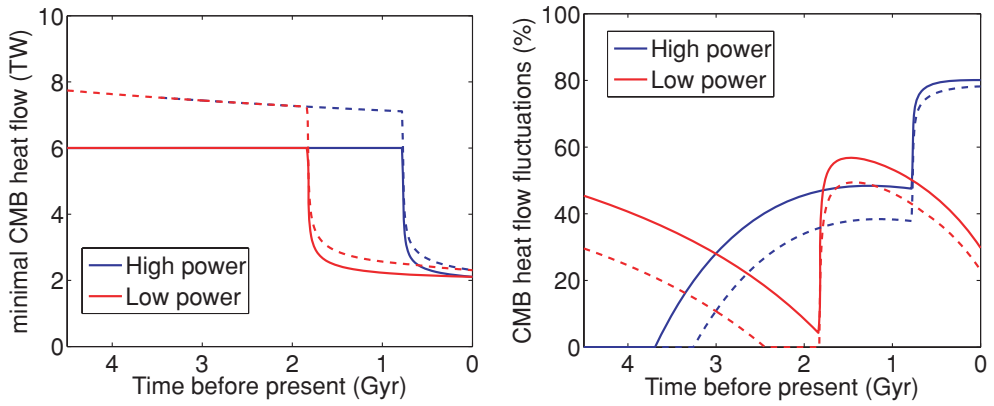

Figure 12. Minimal CMB heat flow (left-hand side: absolute, right-hand side: relative to actual CMB heat flow) needed to get a dynamo (solid lines) and reversals (dashed lines).

a dynamo with about present-day dipolarity, in line with the findings of Roberts & Glatzmaier (2001), Smirnov & Tarduno (2004), and with less frequent reversals than at present, a result which is also in good qualitative agreement with the conclusions of Coe & Glatzmaier (2006), Biggin *et al.* (2008).

Mantle dynamics can cause sizeable temporal fluctuations of the CMB heat flow (see for instance Nakagawa & Tackley 2005), which would superimpose to the long-term geological trend which we used to produce our models. To assess the impact of these fluctuations, we compute in Fig. 12 the minimal CMB heat flow required to get a dynamo. Here it is assumed that $Rm_c = 40$, but this value has a negligible effect on the result, which can be determined by simply writing down the condition $p \geq 0$. If the goal is to maintain a working dynamo throughout the Precambrian, then the low-power scenario appears to impose quite drastic restrictions on the amplitude of allowed fluctuations, especially near the inner core nucleation time, when the dynamo is very close to shut down. In contrast, the high-power scenario allows for fluctuations of 30 per cent and larger throughout the period 3.2 Ga ago to present. The same analysis can be repeated for the onset of reversals, assuming for instance that the critical local Rossby number for reversals is $Ro_{lc}/(1 + \chi) = 0.07$. The thermal dynamo, which pertained to the early Earth conditions would have needed about 1–2 TW superadiabatic CMB heat flow to reverse. Here both scenarios are compatible with the oldest timing for reversals, which is in the range 2.7–3.2 Ga (Strik *et al.* 2003; Tarduno *et al.* 2007). At recent-times, the amount of fluctuations needed to shut down reversals is very close to that needed to shut down the dynamo altogether, a fact which does not support the likeliness of mantle-induced superchrons in the last 500 Myr. Rather, our results would support the idea of superchrons being integral to the variety of timescales spontaneously produced by the dynamo, as suggested by Hulot & Gallet (2003).

The palaeomagnetic predictions derived from the low-power cooling scenario are in fair agreement with palaeomagnetic observables (order of magnitude of the dipole moment, occurrence of reversals). This result confirms that from the perspective of scaling analyses, the power requirement on the geodynamo is fairly economical, as initially suggested by Christensen & Tilgner (2004): the scenario indeed terminates at a dynamo power of only 0.3 TW. Its main drawback is the extreme sensitivity to mantle-induced heat flow fluctuations, which can shut down the dynamo if the heat flow is too close to the critical heat flow required to maintain convection. It is also conflicting with estimates of the present-day CMB heat flow derived from the double crossing of the post-perovskite phase transition (Hernlund *et al.* 2005; Lay *et al.* 2006). These determinations involve an extrapolation of pointwise temperature gradient estimations to the entire lower mantle, and multiplication of the result by the mantle thermal conductivity, both steps being rather uncertain. Such attempts lead to a heat flow lower bound of about 7 TW (van der Hilst *et al.* 2007). Selecting a cooling model, which agrees with this constraint, such as our high-power scenario, does still yield palaeomagnetic predictions in agreement with the observations, while being more permissive on the magnitude of allowed mantle heat flow fluctuations. Note however that such a model necessarily yields higher flow velocities inside the core (Fig. 10b) which are not unrealistic [the conversion factor from surface to deep flow velocities can attain a factor 4 in the study of Christensen & Aubert (2006)] but certainly harder to reconcile with core surface flow velocities of about $5 \times 10^{-4}\,\mathrm{m\,s^{-1}}$. We thus expect that a cooling scenario contained within the bounds represented by our two end-member scenarios would present less consistency problems than either of the end-members.

A striking feature of the recent palaeomagnetic record is the large dispersion of virtual dipole moments (see Fig. 11b), with, for instance, fluctuations from about 2×10^{22} to $15 \times 10^{22}\,\mathrm{A\,m^2}$ in the last 500 Myr, occurring over very short (million year) timescales. These are unlikely to be explained by magnetohydrodynamic processes taking place in dynamo models, where the magnetic field has typically smaller (and faster) fluctuations (see for instance Olson 2008), with epochs of low dipole moment representing only rare events associated with reversals. Moreover, these are also too short to represent a response of the dynamo to changing mantle conditions, and, even if this was the case, the CMB heat flow would have to come very close to the minimal 2 TW required to get a dynamo (Fig. 12) in order to cause such large magnetic field fluctuations. Refinements in the knowledge of CMB heat flow variations, in dynamo theory, and in variability analyses of palaeomagnetic samples, will be needed in order to conclude regarding the physical nature of these variations.

ACKNOWLEDGMENTS

We thank U.R. Christensen for providing the numerical data relative to published dynamo models. JA was supported by CNRS and programs Programme National de Planétologie (PNP) and Structure et Dynamique de l'Intérieur de la Terre (SEDIT) of the French Institut National des Sciences de l'Univers (INSU). SL was supported by program ANR BEGDy from French Agence Nationale

de la Recherche. Numerical calculations were performed at the MésoCentre de Calcul et de données (MCCD) of IPGP, and at IDRIS, France. This is IPGP contribution 2547.

REFERENCES

Aubert, J., Aurnou, J. & Wicht, J., 2008. The magnetic structure of convection-driven numerical dynamos, *Geophys. J. Int.,* **172,** 945–956.

Biggin, A.J., Strik, G.H.M.A. & Langereis, C.G., 2008. Evidence for a very-long-term trend in geomagnetic secular variation, *Nat. Geosci.,* **1**(6), 395–398.

Biggin, A.J., Strik, G.H.M.A. & Langereis, C.G., 2009. The intensity of the geomagnetic field in the late-archaean: new measurements and an analysis of the updated IAGA palaeointensity database, *Earth Planets Space,* **61,** 9–22.

Braginsky, S.I. & Roberts, P.H., 1995. Equations governing convection in Earths core and the geodynamo, *Geophys. Astrophys. Fluid Dyn.,* **79**(1-4), 1–97.

Buffett, B., Huppert, H., Lister, J. & Woods, A., 1996. On the thermal evolution of the Earth's core, *J. geophys. Res.,* **101**(B4), 7989–8006.

Christensen, U. & Aubert, J., 2006. Scaling properties of convection-driven dynamos in rotating spherical shells and application to planetary magnetic fields, *Geophys. J. Int.,* **117,** 97–114.

Christensen, U. & Tilgner, A., 2004. Power requirement of the geodynamo from ohmic losses in numerical and laboratory dynamos, *Nature,* **429,** 169–171, doi:10.1038/nature02508.

Christensen, U.R., 2006. A deep dynamo generating Mercury's magnetic field, *Nature,* **444**(7122), 1056–1058.

Coe, R.S. & Glatzmaier, G.A., 2006. Symmetry and stability of the geomagnetic field, *Geophys. Res. Lett.,* **33**(21), doi:10.1029/2006GL027903.

de Wijs, G., Kresse, G., Vocadlo, L., Dobson, D., Alfe, D., Gillan, M. & Price, G., 1998. The viscosity of liquid iron at the physical conditions of the Earth's core, *Nature,* **392**(6678), 805–807.

Dunlop, D. & Yu, Y., 2004. Intensity and polarity of the geomagnetic field during Precambrian time, in *Timescales of the Paleomagnetic Field,* Vol. 145, pp. 85–100, eds Channell, J.E.T. & Kent, D.V., Lowrie, W. & Meert, J.G., AGU Monograph.

Dunlop, D.J., 2007. Palaeomagnetism—a more ancient shield, *Nature,* **446**(7136), 623–625.

Dziewonski, A. & Anderson, D., 1981. Preliminary reference Earth model PREM, *Phys. Earth planet. Int.,* **25,** 297–356.

Eide, E.A. & Torsvik, T.H., 1996. Paleozoic supercontinental assembly, mantle flushing, and genesis of the Kiaman superchron, *Earth planet. Sci. Let.,* **144,** 389–402.

Hale, C.J., 1987. Paleomagnetic data suggest link between the Archean-Proterozoic boundary and inner-core nucleation, *Nature,* **329**(6136), 233–237.

Hernlund, J.W., Thomas, C. & Tackley, P.J., 2005. Phase boundary double crossing and the structure of Earth's deep mantle, *Nature,* **434,** 882–886, doi:10.1038/nature03472.

Hirao, N., Ohtani, E., Kondo, T., Endo, N., Kuba, T., Suzuki, T. & Kikegawa, T., 2006. Partitioning of potassium between iron and silicate at the core-mantle boundary, *Geophys. Res. Lett.,* **33**(8), doi:10.1029/2005GL025324.

Hulot, G. & Gallet, Y., 1996. On the interpretation of virtual geomagnetic pole (VGP) scatter curves, *Phys. Earth planet. Int.,* **95**(1–2), 37–53.

Hulot, G. & Gallet, Y., 2003. Do superchrons occur without any palaeomagnetic warning? *Earth planet. Sci. Lett.,* **210**(1–2), 191–201.

Kutzner, C. & Christensen, U., 2002. From stable dipolar to reversing numerical dynamos, *Phys. Earth planet. Int.,* **131,** 29–45.

Labrosse, S., 2003. Thermal and magnetic evolution of the Earth's core, *Phys. Earth planet. Int.,* **140,** 127–143.

Labrosse, S., Poirier, J.P. & Le Mouël, J.L., 1997. On cooling of the Earth's core, *Phys. Earth planet. Int.,* **99,** 1–17.

Labrosse, S., Poirier, J.P. & Le Mouel, J.L., 2001. The age of the inner core, *Earth planet. Sci. Let.,* **190**(3-4), 111–123.

Labrosse, S., Hernlund, J.W. & Coltice, N., 2007. A crystallizing dense magma ocean at the base of the Earth's mantle, *Nature,* **450**(7171), 866–869.

Lay, T., Hernlund, J., Garnero, E.J. & Thorne, M.S., 2006. A post-perovskite lens and D″ heat flux beneath the central pacific, *Science,* **314**(5803), 1272–1276.

Lay, T., Hernlund, J. & Buffett, B.A., 2008. Core-mantle boundary heat flow, *Nat. Geosci.,* **1**(1), 25–32.

Lister, J.R., 2003. Expressions for the dissipation driven by convection in the Earth's core, *Phys. Earth planet. Int.,* **140**(1-3), 145–158.

Lister, J.R. & Buffett, B.A., 1995. The strength and efficiency of thermal and compositional convection in the geodynamo, *Phys. Earth planet. Int.,* **91**(1-3), 17–30.

Macouin, M., Valet, J. & Besse, J., 2004. Long-term evolution of the geomagnetic dipole moment, *Phys. Earth planet. Int.,* **147**(2-3), 239–246.

McDonough, W.F., 2003. Compositional model for the Earth's core, in *Treatise on Geochemistry,* pp. 547–569, eds Carlson, R.W., Holland, H.D. & Turekia, D.D., Elsevier, Oxford.

McFadden, P.L., Merrill, R.T., McElhinny, M.W. & Lee, S.H., 1991. Reversals of the earths magnetic-field and temporal variations of the dynamo families, *J. geophys. Res.,* **96**(B3), 3923–3933.

Nakagawa, T. & Tackley, P.J., 2005. Deep mantle heat flow and thermal evolution of the Earth's core in thermochemical multiphase models of mantle convection, *Geophys. Geochem. Geosystems.,* **6,** doi:10.1029/2005GC000967.

Olson, P., 1981. A simple physical model for the terrestrial dynamo, *J. geophys. Res.,* **86**(NB11), 875–882.

Olson, P., 2008. Gravitational dynamos and the low frequency geomagnetic secular variation, *Proc. Natl. Acad. Sci.,* **104**(51), 20 159–20 166.

Olson, P. & Christensen, U.R., 2006. Dipole moment scaling for convection-driven planetary dynamos, *Earth planet. Sci. Let.,* **250**(3-4), 561–571.

Olson, P., Christensen, U. & Glatzmaier, G.A., 1999. Numerical modelling of the geodynamo: mechanisms of field generation and equilibration, *J. geophys. Res.,* **104**(B5), 10 383–10 404.

Pavlov, V. & Gallet, Y., 2001. Middle Cambrian high magnetic reversal frequency (Kulumbe River section, northwestern Siberia) and reversal behaviour during the Early Palaeozoic, *Earth planet. Sci. Let.,* **185**(1-2), 173–183.

Pavlov, V. & Gallet, Y., 2005. A third superchron during the Early Paleozoic, *Episodes,* **28**(2), 78–84.

Perrin, M. & Schnepp, E., 2004. IAGA paleointensity database: distribution and quality of the data set, *Phys. Earth planet. Int.,* **147**(2-3), 255–267.

Rama Murthy, V., Van Westrenen, W. & Fei, Y., 2003. Experimental evidence that potassium is a substantial radioactive heat source in planetary cores, *Nature,* **423,** 163–165.

Roberts, P. & Glatzmaier, G., 2001. The geodynamo, past, present and future, *Geophys. Astrophys. Fluid Dyn.,* **94**(1-2), 47–84.

Secco, R.A. & Shloessin, H.H., 1989. The electrical resistivity of solid and liquid Fe at pressures up to 7 GPa, *J. geophys. Res.,* **94,** 5887–5894.

Smirnov, A. & Tarduno, J., 2004. Secular variation of the Late Archean Early Proterozoic geodynamo, *Geophys. Res. Let.,* **31**(16), doi:10.1029/2004GL020333.

Stacey, F.D. & Loper, D.E., 2007. A revised estimate of the conductivity of iron alloy at high pressure and implications for the core energy balance, *Phys. Earth planet. Int.,* **161**(1-2), 13–18.

Stanley, S., Zuber, M.T. & Bloxham, J., 2007. Using reversed magnetic flux spots to determine a planet's inner core size, *Geophys. Res. Lett.,* **34**(19), doi:10.1029/2007GL030892.

Stevenson, D.J., Spohn, T. & Schubert, G., 1983. Magnetism and thermal evolution of the terrestrial planets, *Icarus,* **54**(3), 466–489.

Strik, G., Blake, T., Zegers, T., White, S. & Langereis, C., 2003. Palaeomagnetism of flood basalts in the Pilbara Craton, Western Australia: Late Archaean continental drift and the oldest known reversal of the geomagnetic field, *J. geophys. Res.,* **108**(B12), doi:10.1029/2003JB002475.

Tarduno, J.A., Cottrell, R.D., Watkeys, M.K. & Bauch, D., 2007. Geomagnetic field strength 3.2 billion years ago recorded by single silicate crystals, *Nature,* **446**(7136), 657–660.

Tauxe, L. & Yamazaki, T., 2007. Paleointensities, in *Treatise on Geophysics. 5- Geomagnetism,* ed. Schubert, G., Elsevier.

Thellier, E. & Thellier, O., 1959. Sur l'intensité du champ magnétique terrestre dans le passé historique et géologique, *Annales de Geophysique,* pp. 285–376.

van der Hilst, R., De Hoop, M.V., Wang, P., Shim, S.-H., Ma, P. & Tenorio, L., 2007. Seismostratigraphy and thermal structure of Earth's core-mantle boundary region, *Science,* **315,** 1813–1817.

Varga, P., Denis, C. & Varga, T., 1998. Tidal friction and its consequences in palaeogeodesy, in the gravity field variations and in tectonics, *J. Geodyn.,* **25**(1-2), 61–84.

Wicht, J., 2002. Inner-core conductivity in numerical dynamo simulations, *Phys. Earth planet. Int.,* **132,** 281–302.

APPENDIX

Here we follow the analysis presented by Lister (2003) to derive an approximate equivalence between dissipation at each boundary and its corresponding mass anomaly flux. Eq. (24) in Lister (2003) gives the original definitions of boundary-originated dissipations Φ_i and Φ_o as they stand in (32) and (35):

$$\Phi_\mathrm{i} = \int_V \mathbf{f_c} \cdot \mathbf{g}\, \mathrm{d}V + Q^*_\mathrm{ICB}[1 - \overline{T}/T_\mathrm{o}(r_\mathrm{i})] \tag{A1}$$

$$\Phi_\mathrm{o} = Q^*_\mathrm{CMB}[1 - \overline{T}/T_\mathrm{o}(r_\mathrm{i})]. \tag{A2}$$

Here $\mathbf{f}_\mathrm{c}$ is the convective compositional mass anomaly flux, T_o is the adiabatic temperature gradient, $\overline{T}$ is the mass-averaged temperature in the shell, $Q^*_\mathrm{ICB,CMB}$ are the superadiabatic heat flows at inner-core boundary and CMB. The last term in eq. (24) of Lister (2003) is neglected because the average temperature of dissipation is assumed to be $\overline{T}$. Denoting the compositional mass anomaly flux at the inner core boundary as F_{ci}, and assuming, as in Lister (2003) that compositional diffusion can be neglected and that the convective (not total) compositional flux is well mixed throughout the shell, we have $\nabla \cdot \mathbf{f}_\mathrm{c} = F_{ci}/V$ and an integration by parts of the first term in (A1) yields

$$\int_V \mathbf{f_c} \cdot \mathbf{g}\, \mathrm{d}V \approx F_{ci}(\psi_\mathrm{i} - \overline{\psi}). \tag{A3}$$

Integrating the definition of the adiabatic temperature gradient and neglecting the radial variations of α and the heat capacity C_p, we have

$$\frac{\alpha}{C_p}(\psi(r) - \psi_\mathrm{i}) = \ln[T_\mathrm{o}(r)/T_\mathrm{o}(r_\mathrm{i})]. \tag{A4}$$

Under the assumption of moderate departure of T_o from the mass-averaged temperature $\overline{T}$ and of moderate density variations, the mass average of the previous equation yields

$$\frac{\alpha}{C_p}(\psi_\mathrm{i} - \overline{\psi}) \approx [1 - \overline{T}/T_\mathrm{o}(r_\mathrm{i})] \tag{A5}$$

and we have therefore

$$Q^*_\mathrm{ICB}[1 - \overline{T}/T_\mathrm{o}(r_\mathrm{i})] \approx F_{ti}(\psi_\mathrm{i} - \overline{\psi}), \tag{A6}$$

where F_{ti} is the thermal mass anomaly flux at the inner boundary. From here it is apparent that Φ_i as it stands in (32) corresponds to Φ_i as used in (15), the same result holding for Φ_o. As discussed in Lister (2003), the accuracy of the various approximations used in this derivation reduce to that of the Boussinesq approximation.